Identification of damage states of load-bearing rocks using infrared radiation monitoring methods

Gao, Qiangqiang; Ma, Liqiang; Liu, Wei; Wang, Hui; Ma, Qiang; Wang, Xiuzhe

DOI
10.1016/j.measurement.2024.115507

Publication date
2024

Document Version
Final published version

Published in
Measurement: Journal of the International Measurement Confederation

Measurement 239 (2025) 115507

Contents lists available at ScienceDirect

Measurement

journal homepage: www.elsevier.com/locate/measurement

Identification of damage states of load-bearing rocks using infrared radiation monitoring methods

Qiangqiang Gao [a], Liqiang Ma [a,b,c,d,*], Wei Liu [a], Hui Wang [a], Qiang Ma [a], Xiuzhe Wang [e]

[a] School of Mines, China University of Mining and Technology, Xuzhou, Jiangsu 221116, China
[b] Key Laboratory of Xinjiang Coal Resources Green Mining (Xinjiang Institute of Engineering), Ministry of Education, Urumqi 830023, China
[c] Xinjiang Key Laboratory of Coal-bearing Resources Exploration and Exploitation, Xinjiang Institute of Engineering, Urumqi 830023, China
[d] Xinjiang Engineering Research Center of Green Intelligent Coal Mining, Xinjiang Institute of Engineering, Urumqi 830023, China
[e] Faculty of Civil Engineering and Geoscience, Delft University of Technology Stevinweg 1, Delft 2628CN, Netherlands

ARTICLE INFO

Keywords:
Damage evolution state
Infrared radiation monitoring
Convolutional neural network (CNN)
Dataset
Online monitoring

ABSTRACT

The online identification of rock damage states is crucial for safety monitoring in geotechnical and mining engineering. By analyzing spatiotemporal evolution patterns of infrared radiation in various rock damage states, we established the first infrared temperature field dataset for rock damage state identification. We then constructed a deep convolutional neural network, RESD-CNN, and performed its training and optimization. Results showed that infrared radiation patterns of different rock samples exhibit similarities. RESD-CNN achieved outstanding performance in identifying rock damage states with metrics of ACC 99.04%, Precision 99.39%, Recall 99.52%, and F1-score 99.46% on the validation set. Generalization tests on datasets of different rock types revealed that RESD-CNN significantly outperformed traditional classification methods, demonstrating the feasibility of infrared radiation technology for intelligent coal rock damage identification. This research provides a crucial foundation for developing online identification and early warning systems for rock damage evolution in engineering.

1. Introduction

Engineering safety is closely related to the safety of people's lives and properties. The destabilization damage of mining, caverns, tunnels, bridges, and buildings is all caused by the evolution of internal damage of geotechnical materials under stress [1–6]. Under stress, the rock interior is accompanied by the closure, sprouting, expansion, and reciprocal penetration of cracks. The mechanical properties of the rock are closely related to the development of microcracks in its interior [7–10]. The crack development process inside the rock can be divided into stages and bounded by four strength characteristics, which are compression density strength (σ_{cc}), crack initiation strength (σ_{ci}), damage strength (σ_{cd}), and peak strength (σ_f). Therefore, it is important to study the process and mechanism of rock damage evolution, to judge the state of damage evolution, to evaluate the degree of damage, and to warn the damage destabilization for the prevention of rock engineering disasters [11–18]. It can lay the foundation for the research and development of real-time monitoring, identification, and early warning systems of damage evolution state in actual rock engineering.

In recent decades, the determination methods of rock damage evolution state mainly include stress–strain curve determination method, volume strain method, crack volume strain method, acoustic emission method, moving point regression method, etc., which can be further summarized as strain method and acoustic emission method. Martin et al. [19] proposed the use of crack volume strain versus axial strain to find the crack initiation stress, which has the advantage of objectivity and is now more mature. However, the difficulty of this method lies in the determination of elastic parameters such as modulus of elasticity and Poisson's ratio, which are very sensitive to the results. Eberhardt et al. [20] used the moving point regression technique in relation to the average axial stiffness and axial stress to find the crack initiation stress, which reduces the subjectivity, but still faces difficulties in judging the estimated elastic parameters. Tang et al. [21] proposed the use of the relationship between the lateral strain response direction, a more stable lateral strain interval response method was proposed to determine the crack initiation stress. In addition, the acoustic emission method is

* Corresponding author at: Key Laboratory of Xinjiang Coal Resources Green Mining (Xinjiang Institute of Engineering), Ministry of Education, Urumqi 830023, China.

E-mail address: ckma@cumt.edu.cn (L. Ma).

https://doi.org/10.1016/j.measurement.2024.115507
Received 13 June 2024; Received in revised form 30 July 2024; Accepted 10 August 2024
Available online 12 August 2024

considered to be a practical method. Martin et al. [19] used the first and second inflection points of the acoustic emission event rate cumulative curves that deviate from the straight line as the identification criterion for crack initiation strength and damage strength. Amann et al. [22] and Eberbaradt et al. [20] found that only a small number of acoustic emission events were generated before the cracking intensity point and that the acoustic emission events increased significantly when loading reached the cracking intensity. The first inflection point of the acoustic emission event accumulation curve was then proposed as a basis for determining the fracture initiation strength. Zhao et al. [23] selected the starting point of the first deviation from the linear section of the acoustic emission parameter curve as the crack initiation strength point. After reaching the damage strength, the acoustic emission parameter curve increased rapidly, and the intersection of the two linear extension lines of the acoustic emission parameter accumulation curve was used as the damage strength point.

The above research has made an active exploration of the determination of rock damage state through rock strain and acoustic emission tests. However, due to the complexity of rock materials, the influence of rock structure, composition and other factors, it is still difficult to identify the rock damage state. In the field of rock mechanics, acoustic emission [24,25], SEM [26], CT [27], resistivity[28], X-ray[29], ultrasonic [24,30,31], and so on are widely used in the study of rock damage evolution characterization and evaluation. Compared with the above methods, infrared radiation (IR) monitor technology has the advantages of real-time, non-destructive, non-contact, low cost, simple operation, and wide monitoring range. It is an ideal monitoring method for rock damage evolution, and has great application potential in damage detection and disaster prevention of rock materials [32–38]. Wu et al. [39,40] analyzed the typical AIRT and infrared temperature matrix evolution characteristics of rock samples under various loading conditions, and discussed the generation mechanism of infrared radiation in the process of rock damage and fracture. They pointed out that the change of infrared radiation in the process of rock damage evolution is mainly controlled by frictional thermal effect and thermoelastic effect. Wang et al.[41] found the damage prediction point of limestone by the infrared radiation temperature curve and the evolution of the infrared temperature matrix. Through the acoustic-electric-thermal multi-parameter experiment of coal rock, it is found that the infrared temperature contour map at different time points can better reflect the evolution process of the surface temperature field of the sample, and it is considered that the failure of the sample originates from local failure. Li et al. [42] found that the infrared radiation precursor characteristics. They concluded that the infrared radiation temperature contour map and IR image cloud map can reflect the occurrence, expansion, rupture location, and evolution process of cracks in time and space, which can be used to predict the deformation damage form and intensity of gas-containing coal, and accurately locate the position of the coal-rock dynamics disaster. Huo et al. [43] and Lin et al. [44] investigated the damage mechanism and temperature field evolution trend of rockbursts under different stress gradient loading, and found the infrared radiation precursor characteristics of rockbursts generated under different stress gradients. Li et al. [42,45,46] concluded that infrared radiation temperature contour maps and IR image cloud maps can reflect the occurrence, and expansion of cracks in time and space, Cao et al. [47] studied the average infrared radiation temperature (AIRT) characteristics of the rock shear expansion process. Liu et al. [48] found the infrared radiation b-value with reference to the acoustic emission b-value for the first time, and quantitatively analyzed the change characteristics of the infrared radiation b-value in the process of rock rupture. Shen et al. [49] investigated the precursor points of coal-rock rupture based on the information of infrared radiation by using the theory of critical slowing down.

Most of the above studies focus on the description of the changing law of infrared radiation in the process of carrying coal rock damage and rupture, which is a good discovery of the precursor points of infrared radiation in coal rock rupture. However, in the actual engineering, people are more concerned about which damaged state the coal rock is in. Therefore, combining the advantages of infrared radiation monitoring technology, it is necessary to research the identification and evaluation of rock damage damage state.

Artificial intelligence methods are widely used in rock engineering fields such as rock mass classification [50], coal-rock interface identification [51], rock strength estimation [52], landslide prediction [53], etc. This is due to the approximation and fitting ability of artificial intelligence methods to complex nonlinear function relations. In this paper, four kinds of rocks, yellow shale, limestone, yellow sandstone, and coal, were subjected to uniaxial loading infrared radiation observation experiments. The basic mechanical characteristics of four kinds of rocks and the temporal and spatial evolution of infrared radiation in different damage states are studied. The infrared temperature matrix data set of rock damage state recognition is established. The convolutional neural network method is used to classify and predict the rock damage state. The research content can lay a foundation for the real-time monitoring, identification and early warning system of damage evolution state in actual rock engineering.

2. Rock infrared thermographic data acquisition

2.1. Experimental design

2.1.1. Specimen preparation

In this paper, four specimens of yellow shale, limestone, yellow sandstone, and coal were subjected to uniaxially loaded infrared radiation monitoring experiments (Fig. 1). Each specimen was selected from a whole block of rock (coal) with no obvious geological defects to minimize the variation of physical properties in the specimens. The specimens were processed in strict accordance with the requirements of the International Society of Rock Mechanics. All specimens were machined as rectangles of 50 mm × 50 mm × 100 mm. Among them, the error of unevenness of two end faces is less than 0.05 mm, and the error of unparallelism of each end face is less than 0.02 mm. Four pieces each of yellow shale, limestone, yellow sandstone, and coal are labeled as A_i, B_i, C_i, and D_i, where i = 1,2,3,4. The basic physical and mechanical parameters of each specimen are shown in Table 1. The average densities of yellow shale, limestone, yellow sandstone, and coal are 2728.57 kg/m^3, 2712.4 kg/m^3, 2465.95 kg/m^3, and 1390.82 kg/m^3, respectively.

2.1.2. Experimental system and experimental procedure

The experimental apparatus used is shown in Fig. 1. The loading equipment is MTS C64.106 electro-hydraulic servo universal testing machine, the maximum load is 1000kN; the measurement accuracy of the testing machine is ± 0.5 %; the deformation measurement accuracy is ± 0.5 %; the displacement measurement accuracy is ± 0.5 %. The displacement control loading method is adopted, the loading rate is 0.2 mm/min, and the acquisition frequency of the testing machine is 10 times/second. The infrared observation equipment is the model VarioCAM HD head 880 uncooled infrared camera produced by InfraTec, Germany. The main parameters of the camera are as follows: the temperature measurement range is −40℃-1200℃, the temperature sensitivity is 0.02℃, the image resolution is 1240 × 768, the maximum image acquisition frequency is 30fps, and the measurement band is 7.5–14 μm. In this experiment, the acquisition frequency of the infrared camera is 10 fps, and the static resistance strain gauge model TS3890N is used, with a resolution of ± 1 με; the accuracy is ± 0.5 %, ±3 με; the measurement range is 0~±20,000 με; the sampling rate is 10 points/second.

Strain gauges were pasted on the surface of all specimens according to the experimental specifications as shown in Fig. 1. Then all specimens were placed in the laboratory 24 h in advance so that the temperature of the specimens was the same as the temperature in the laboratory. Before starting the experiment, a reference specimen was placed at a distance of about 8 cm from the loaded specimen, so that the loading was at the

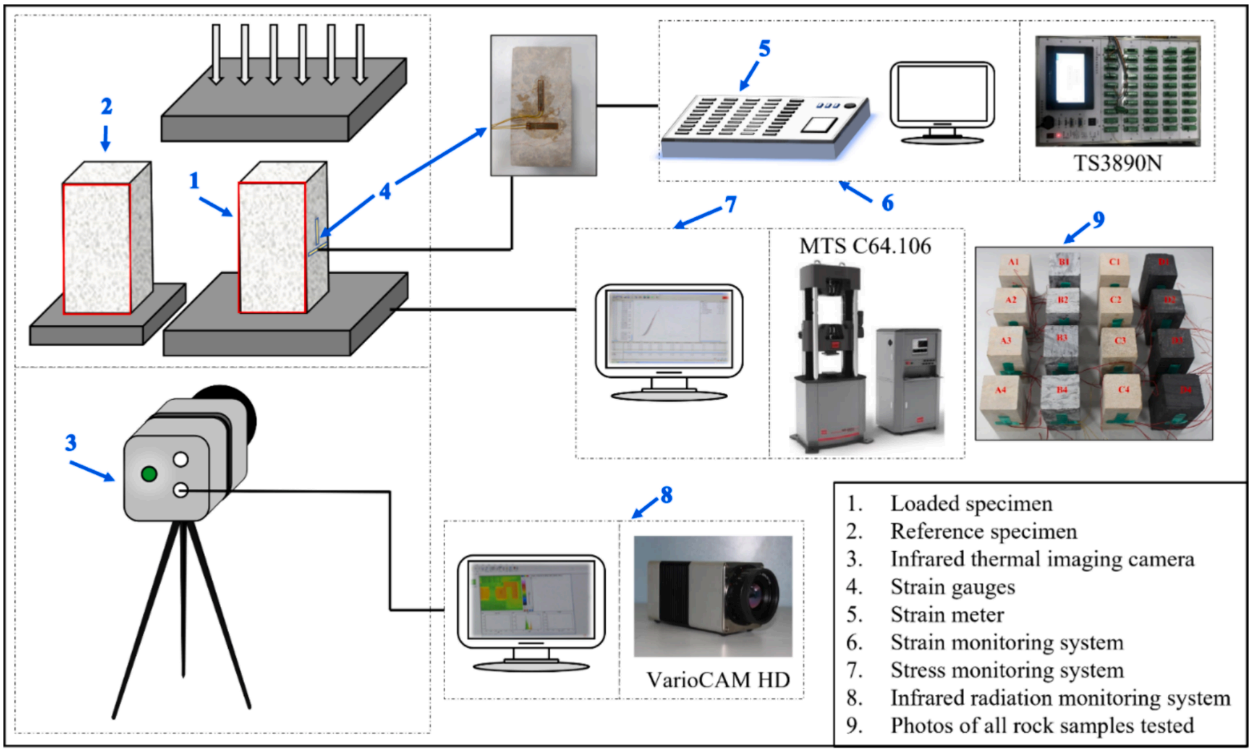

Fig. 1. Equipment physical diagram, test schematic diagram, and test rock sample photos.

same height and flush with the reference specimen. To reduce end effects and heat transfer effects, an insulating sheet of plastic was placed between the two ends of the specimen in contact with the press. The specimen is left for 10 min and after the surface temperature of the sample is uniform, the press is manually controlled and the loaded specimen is preloaded with a force of 1 kN. After that, the press, the IR imaging camera, and the strain monitor were started at the same time to begin the experiment. During the whole experimental operation, the experimental personnel wore adiabatic gloves, the laboratory was closed, and no one was allowed to walk around the laboratory after all the instruments started working.

2.2. IR image preprocessing

In the infrared radiation information acquisition process, it will be accompanied by a lot of noise information, including background thermal noise, temporal noise from non-uniformity correction of non-cooled thermal imaging cameras [32], as well as ambient temperature heat transfer, thermal radiation, thermal convection, and heat transfer between the contact surface of the specimen and the press [54,55]. In order to perform noise correction of the thermal image, a reference specimen is set up in this paper [32,56,57]. And the acquired thermal image data are processed as follows.

a. Background thermal noise filtering was performed on the IR image of the loaded specimen using the reference specimen IR image, i.e.

$$F(x,y)_t = L(x,y)_t - R(x,y)_t \tag{1}$$

where L(x,y)t denotes the thermogram temperature matrix of the loaded specimen at time t. R(x,y)t denotes the thermogram temperature matrix of the reference specimen at time t. F(x,y)t denotes the temperature matrix of the loaded specimen at time t after denoising. Where, (x,y) denotes the position coordinates of the temperature matrix and t denotes the moment. It is worth noting that $x \in [1,100]$,$y \in [1,200]$.

b. To reduce the effect of temporal noise on the thermogram sequence, multi-frame cumulative averaging denoising was performed for $F(x,y)_t$ according to Liu et al [32]. The expression is

$$G(x,y) = \frac{1}{m}\sum_{(n-1)m+1}^{nm} F(x,y), n = 1,2,\cdots,[p_{\max}/m] \tag{2}$$

where G(x,y) denotes the matrix after multi-frame cumulative averaging denoising, m is the number of frames per multi-frame cumulative averaging denoising, and pmax is the maximum number of frames of F (x,y). In this paper, for the convenience of analysis, m is set to 10, and the thermal image sequence of loaded specimens for integer seconds is obtained.

2.3. Statistics of rock characteristic strength

Deformation damage of rocks is a gradual process, involving the closure, sprouting, expansion, and aggregation of cracks into nuclei. The rock loading process goes through several stages: the initial compaction stage, the elastic deformation stage, the stable development of cracks, the unstable development of cracks, and the post-peak damage stage (Fig. 4). The development and evolution patterns of cracks in each stage differ, resulting in varying stress–strain curves. Four stress thresholds are commonly used to classify the different damage stages: compaction strength, crack initiation strength, damage strength, and peak strength (Fig. 4). Scholars have conducted numerous studies on methods for determining these stress thresholds, mainly the strain method and the acoustic emission method. Among these, the crack volume strain method proposed by Martin et al. [19] is widely used due to its relatively clear physical meaning. The crack volume strain method divides the volumetric strain of the rock into elastic volumetric strain and crack volumetric strain. In uniaxial compression, the total volumetric strain of the specimen is defined as:

$$\varepsilon_v = \varepsilon_1 + 2\varepsilon_2 \tag{6}$$

where ε_v denotes the total volume strain, ε_1 denotes the axial strain, and ε_2 denotes the transverse strain. The elastic volumetric strain is defined as:

Table 1
Basic physical and mechanical parameters of the specimen.

Specimen No.	A_1	A_2	A_3	A_4	B_1	B_2	B_3	B_4	C_1	C_2	C_3	C_4	D_1	D_2	D_3	D_4
E (GPa)	12.10	11.51	12.55	10.10	9.36	11.99	10.56	7.91	9.29	7.32	10.36	8.53	2.80	2.15	1.54	1.51
μ	0.24	0.28	0.23	0.17	0.17	0.28	0.23	0.24	0.23	0.21	0.19	0.20	0.26	0.24	0.24	0.28
Density(kg/m^3)	2733.29	2741.79	2743.74	2695.44	2694.62	2739.27	2675.54	2740.18	2394.32	2475.51	2488.70	2505.30	1472.46	1445.34	1342.36	1303.09

$$\varepsilon_v^e = \frac{1-2\mu}{E}\sigma \tag{7}$$

where ε_v^e denotes the elastic volume strain, σ denotes the stress, and μ and E denote poisson's ratio and elastic modulus, respectively. The crack volume strain is defined as the difference between the total volume strain and the elastic volume strain. That is.

$$\varepsilon_v^c = \varepsilon_v - \varepsilon_v^e \tag{8}$$

where, ε_v^c denotes the crack volume strain.

The characteristic strength, volume strain, and crack volume strain curves in the full uniaxial compression curve of specimen B2 are shown in Fig. 2. Biniawski et al. [58,59] divided the rock loading stages into initial compaction stage (I), elastic deformation stage (II), crack stable development stage (III), unstable crack development stage (IV), and post-peak damage stage (V) according to the characteristic strength. Within stage I, the rock primary joints, cracks, and fissures are compacted under the action of external forces. In stage II, the rock is deformed elastically under the action of external forces, no new cracks are generated internally, and the slope of the stress–strain curve does not change. In stage III, new microcracks begin to develop inside the rock under the action of external forces. In stage IV, a large number of microcracks develop and expand inside the rock, and crack penetration occurs locally until the peak stress is reached. Entering stage V, the stress gradually decreases, through cracks appear on the rock surface, and rock damage occurs. In the elastic loading stage, the crack volume strain curve exhibits a horizontal line segment. This horizontal segment occurs because, during this phase, the deformation of the rock is primarily elastic. Therefore, the volume strain due to crack expansion is minimal and does not significantly contribute to changes in crack volume strain. Essentially, the crack volume strain remains stable, which is reflected in the horizontal nature of the curve. The start of this segment represents the compression density strength, while the end denotes the crack initiation strength, marking the transition to the stage where significant crack expansion begins. Cai et al. [60] proposed that the damage strength can be determined by the peak inflection point of the volumetric strain, at which the rock begins to expand. As shown in Table 1, the characteristic strength points of each specimen in this study were determined using the crack volume strain model method. According to the experimental results, the range of σ_{cc}/σ_f for all specimens is 20.25 %–35.53 %, σ_{ci}/σ_f is 41.97 %–69.47 %, and σ_{cd}/σ_f is 78.84 %–94.84 %.

3. Results and analysis

3.1. Spatial variation characteristics of IR of rock damage evolution

In this paper, four different rock samples were subjected to uniaxial loading infrared radiation observation experiments, and the infrared radiation characteristics of different rock samples were similar. It should be noted that the IR imager detects the radiation intensity of the rock surface and converts it into a temperature field according to the Boltzmann equation. Therefore, the emissivity of the rock surface is more sensitive to the experimental results. Due to the small area of the sample, the emissivity of all rock samples is the same, which is reasonable for the qualitative analysis of the temperature field.

The IR image can visually display the spatial distribution of the surface temperature field of the sample. Due to the limitation of space, this paper draws the thermal images of A_1、B_2、C_3、D_4 samples at the characteristic intensity points, and analyzes the spatial distribution of radiation temperature.

The infrared thermograms corresponding to the four specimens A_1, B_2, C_3, and D_4 at the characteristic intensity values are shown in Fig. 3. At the beginning of the experiment for 1 s, the infrared radiation temperature distribution on the rock surface was relatively uniform, and all of them were in the low temperature range. As the loading proceeds, the

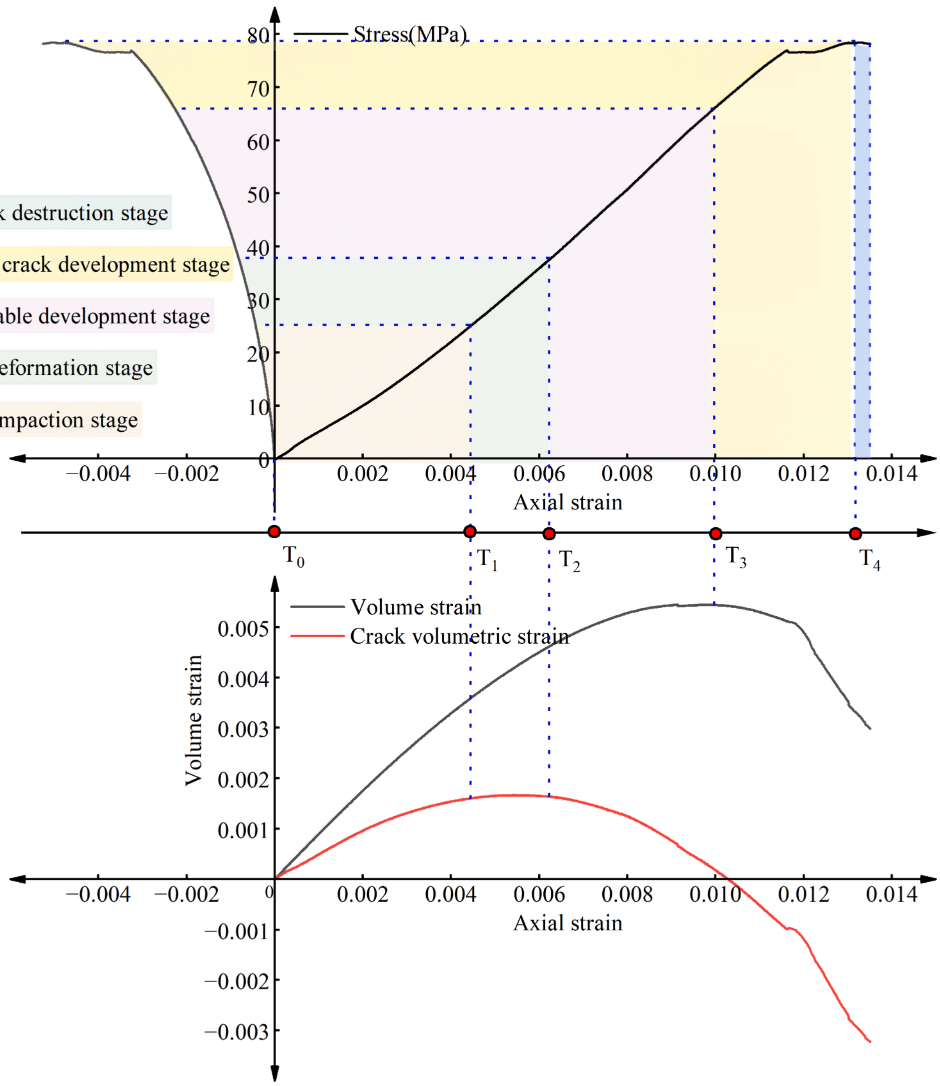

Fig. 2. Plots of characteristic strength, volume strain and crack volume strain curves of B_2 specimen during the whole process of uniaxial compression.

stress reaches the compaction strength, at which time, the thermal image shows that the infrared radiation temperature diverges, and the high-temperature point gradually increases, but the range is small. When the stress reaches the crack initiation strength, the high-temperature points on the surface of the rock sample increase. It is worth noting that the radiation temperature of the whole rock surface is relatively increased. When the stress reaches the damage strength, the temperature on the surface of the rock sample further increases, and a high-temperature concentration area appears (the yellow and red parts in Fig. 3). When the stress reaches the peak strength, the low temperature zone is less and less, and the high-temperature concentration zone is more obvious (A_1, B_2, C_3 in Fig. 3). For D_4, when the stress reaches the peak strength, the high-temperature region decreases, and a relatively low-temperature band is generated. This is because at the peak strength, macroscopic penetrating cracks are generated on the surface of the coal sample, and a large number of low-temperature backgrounds appear in the region (red oval in D_4).

It can be seen that during the loading process of the rock sample, the surface radiation temperature shows a trend of decreasing low-temperature points and increasing high-temperature points, and is accompanied by the appearance of high-temperature concentration areas. The high-temperature concentration area is mainly distributed in the central region of the rock sample surface, mainly because this region is the main area of crack development. This is the same as the conclusion obtained from the literature [41].

3.2. *Infrared radiation time variation characteristics of rock damage evolution*

The infrared thermal image captures the spatial distribution of surface temperature, making it challenging to discern the temporal variation characteristics of infrared radiation temperature. The average infrared radiation temperature (AIRT) of the rock surface represents the mean value of the temperature matrix from the infrared thermal image. This is a widely used quantitative index for infrared radiation information. As shown in Fig. 4, the stress and AIRT curves for the four samples (A_1, B_2, C_3, and D_4) over time are depicted. It can be observed that AIRT exhibits a clear periodic variation trend.

In the initial compaction stage (I), the stress level is low, the primary pores and micro-cracks of the sample are gradually closed, and AIRT does not show a clear change trend. After the initial AIRT of A_1 and C_3 samples floated up and down for a period of time, there was a significant decrease. The AIRT of the B_2 sample fluctuates slightly, and the AIRT of the D_4 sample rises after a period of time.

In the elastic deformation stage (II), the sample undergoes linear elastic deformation, and AIRT increases with the increase of stress. In this stage, the development of new cracks is less, and the rock mainly undergoes elastic deformation. The change of AIRT is mainly related to

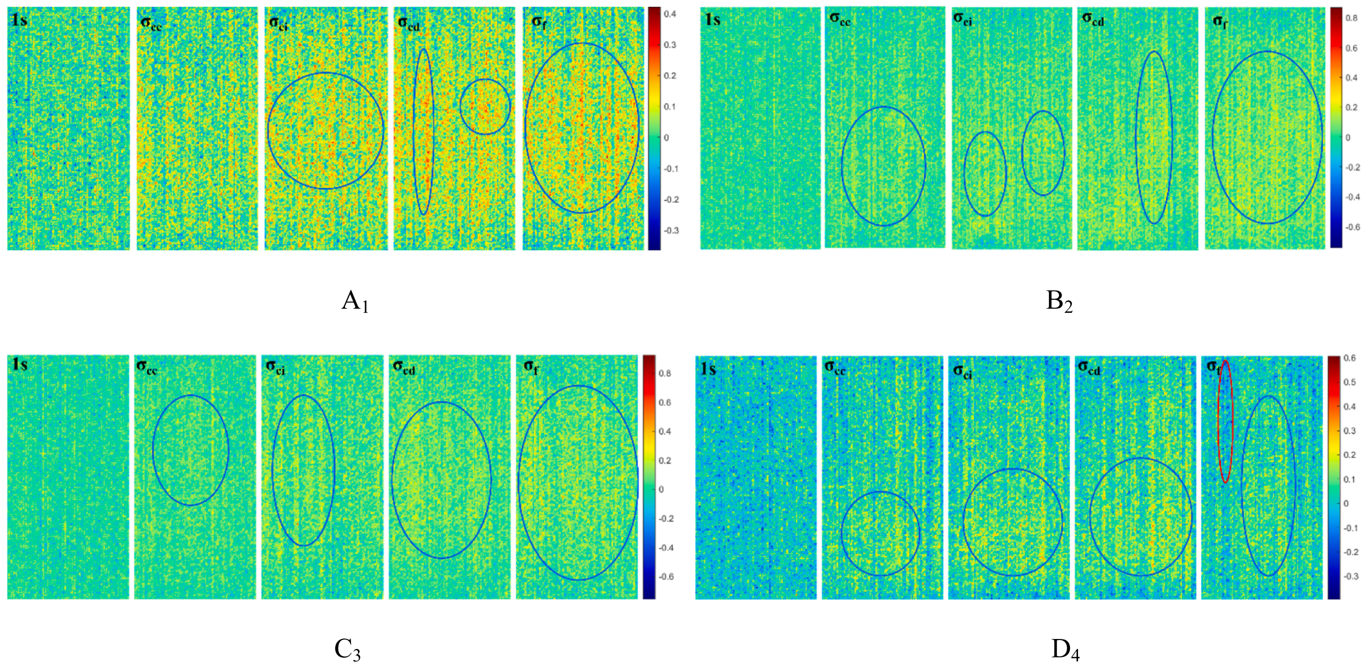

Fig. 3. Infrared thermogram corresponding to the characteristic stress value.

the thermoelastic effect.

In the stage of stable crack development (III), the stress reaches the crack initiation strength, and the internal microcracks begin to germinate. Friction occurs between rock particles, new cracks and microcracks, and AIRT rises rapidly in this stage.

In the unstable development stage of crack (IV), under the action of stress, the internal cracks and microcracks of rock expand, penetrate and nucleate, and some structures are unstable and destroyed. AIRT has two cases in this stage. One is that the internal structure is unstable, which leads to the initial decrease of stress. At this time, AIRT is also greatly reduced accordingly, such as A_1 and D_4. Among them, D_4 phenomenon is more obvious, and AIRT decreases linearly. In the second case, the internal bearing capacity of the sample is strong, and there is no stress drop. As shown in Fig. B2 and C3, AIRT has no obvious sudden drop, and AIRT continues to increase with the development of internal microcracks. After that, the rock enters the post-peak failure stage. Due to the strong brittleness of the sample, the post-peak failure stage lasts for a short time. With the failure of the rock sample, AIRT is greatly reduced.

The infrared thermograms of different rocks in different stages of damage evolution have similar characteristics, i.e., the stage evolution of the infrared radiometric sequence of rocks. However, it is difficult for the human eye to make an objective and correct judgment of the rock damage evolution status based on the changing characteristics of the infrared thermogram during the rock damage evolution. Convolutional neural network (CNN) has powerful fitting and approximation ability for complex nonlinear functional relations, so it can be used to determine the damage evolution state of rocks.

3.3. Infrared radiation identification of rock damage evolution state

3.3.1. Establishment of IR image data set

Through the crack strain model method (Section 2.3), different damage evolution stages of different rocks can be identified, namely, initial compaction stage, elastic deformation stage, crack stable development stage and crack unstable development stage. Each stage is divided according to the time nodes corresponding to the three characteristic strengths (σ_{cc}, σ_{ci}, σ_{cd}). As shown in Fig. 4, the time periods corresponding to the four stages are: 0–T1, T1–T2, T2–T3, T3–T4. T1, T2, T3, and T4 are the time corresponding to σ_{cc}, σ_{ci}, σ_{cd} and σ_f, respectively. The time of all samples is shown in Table 2. According to the time node, the IR image in (0, T1] is divided into the initial compaction stage thermal image, similar to the thermal image in (T1, T2], (T2, T3], (T3, T4], which are the thermal image of elastic deformation stage, the thermal image of crack stable development stage and the thermal image of crack unstable development stage. The number of thermal images of all samples at each stage is shown in Table 3.

Through Table 3, it is found that the number of thermal images of all samples is 10,322, and the total number of thermal image data sets of stage I, stage II, stage III and stage IV is 5940, 1865, 1445, and 1072 respectively. Because the number of thermal images of stage I is too large (about 57.55 % of the total number), the data set is extremely unbalanced, so the thermal images of stage I of each sample are sampled at intervals. The method is as follows: According to the time series sequence of IR images, the thermal images of even seconds in the (0, T1] time period are removed in turn, and the thermal images of odd seconds are retained. The total number of rock IR images after sampling is 7357, of which the number of stage I, stage II, stage III, and stage IV accounts for 40.44 %, 25.35 %, 19.64 %, and 14.57 % respectively. It is worth noting that the size of all images is 200*100.

3.3.2. RDES-CNN architecture

CNN is mainly composed of the input layer, hidden layer, and output layer, the hidden layer contains multiple convolutional layers, a pooling layer, and a fully connected layer and activation function. Among them, CNN is characterized by parameter sharing, compared with traditional neural networks, CNN has the advantage of fewer parameters and connections and proposes the idea concept of local receptive field, which has a greater advantage for image feature extraction. In CNN, the convolution layer performs convolution operation on the input rock infrared temperature matrix through a series of fixed-size convolution kernels to extract the features of the image. The pooling layer performs feature aggregation on the feature maps output from the convolutional layer, which reduces the dimensionality of the feature maps, reduces the number of parameters of the network, and shortens the training time of the model. The fully connected layer then converts the feature maps obtained after multiple convolution and pooling operations into one-dimensional vectors, and generates probability distributions through the Softmax activation function to finally determine the classification of

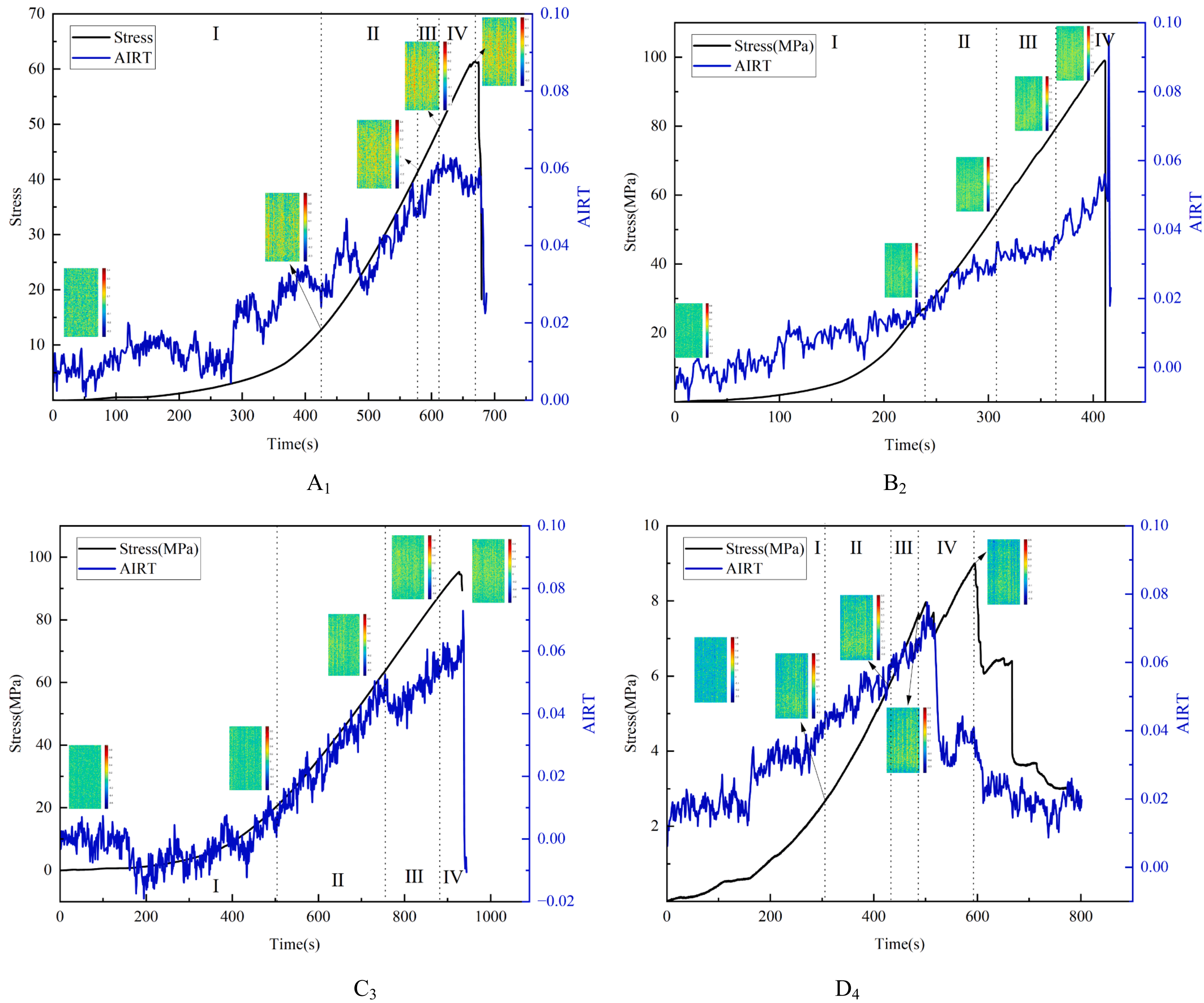

Fig. 4. Plot of stress, AIRT vs. time for the specimen.

Table 2
Characteristic strength values of each specimen.

Specimen No.	σ_{cc} (MPa)	σ_{ci} (MPa)	σ_{cd} (MPa)	σ_f (MPa)	σ_{cc}/σ_f	σ_{ci}/σ_f	σ_{cd}/σ_f	Time points corresponding to feature strength (s)			
								T_1	T_2	T_3	T_4
A1	12.66	42.40	49.80	61.31	20.65 %	69.16 %	81.23 %	424.2	582.5	614.2	669.0
A_2	20.46	33.69	63.05	71.71	28.53 %	46.98 %	87.92 %	388.2	457.0	581.9	625.6
A_3	22.00	46.06	57.64	73.11	30.09 %	63.00 %	78.84 %	497.1	612.6	662.4	737.9
A_4	12.89	26.48	45.04	54.79	23.53 %	48.33 %	82.20 %	296.7	377.8	465.2	514.3
B_1	19.96	38.73	66.15	77.48	25.76 %	49.99 %	85.38 %	233.3	296.1	367.4	401.0
B_2	27.61	55.86	79.81	99.06	27.87 %	56.39 %	80.57 %	240.4	309.5	365.3	411.0
B_3	21.00	43.53	84.59	103.71	20.25 %	41.97 %	81.56 %	319.8	389.3	499.6	551.2
B_4	19.30	40.04	66.45	82.23	23.47 %	48.69 %	80.81 %	267.9	342.4	417.4	462.9
C_1	21.73	48.99	62.60	72.42	30.01 %	67.65 %	86.44 %	424.3	587.3	660.5	730
C_2	24.99	37.76	65.96	78.41	31.87 %	48.16 %	84.12 %	410.0	486.7	635.9	721.1
C_3	20.58	59.29	85.92	95.33	21.58 %	62.19 %	90.13 %	503.9	731.5	871.0	927.0
C_4	33.18	52.60	75.51	93.38	35.53 %	56.33 %	80.86 %	358.0	423.3	492.4	560.1
D_1	8.08	15.20	21.62	25.34	31.89 %	59.98 %	85.32 %	505.0	658.3	794.0	894.8
D_2	4.52	10.42	14.23	15.00	30.13 %	69.47 %	94.87 %	368.4	565.9	692.0	726.7
D_3	5.24	10.52	13.94	16.24	32.27 %	64.78 %	85.84 %	399.3	554.7	650.8	798.1
D_4	2.71	5.92	7.57	9.00	30.11 %	65.78 %	84.11 %	307.4	435.3	484.6	594.6

Table 3
Infrared thermograms of each specimen at each stage.

Specimen No.	stage I		stage II	stage III	stage IV	Before sampling		After sampling	
	Number	After interval sampling	Number	Number	Number	Total	Ratio	Total	Ratio
A_1	425	213	158	32	55	670	6.49 %	458	6.23 %
A_2	388	194	69	124	44	625	6.06 %	431	5.86 %
A_3	497	250	115	50	75	737	7.14 %	490	6.66 %
A_4	296	148	81	88	49	514	4.98 %	366	4.97 %
B_1	233	117	63	71	34	401	3.88 %	285	3.87 %
B_2	240	120	69	56	46	411	3.98 %	291	3.96 %
B_3	319	160	70	110	52	551	5.34 %	392	5.33 %
B_4	267	134	75	75	45	462	4.48 %	329	4.47 %
C_1	424	212	163	73	70	730	7.07 %	518	7.04 %
C_2	410	205	76	149	86	721	6.99 %	516	7.01 %
C_3	504	252	228	140	56	928	8.99 %	676	9.19 %
C_4	358	179	65	69	68	560	5.43 %	381	5.18 %
D_1	505	253	153	136	100	894	8.66 %	642	8.73 %
D_2	368	184	197	127	34	726	7.03 %	542	7.37 %
D_3	399	200	155	96	148	798	7.73 %	599	8.14 %
D_4	307	154	128	49	110	594	5.75 %	441	5.99 %
Total	5940	2975	1865	1445	1072	10,322	\	7357	\
Ratio (Before sampling)	57.55 %	\	18.07 %	14.00 %	10.39 %	\	\		\
Ratio (After sampling)		40.44 %	25.35 %	19.64 %	14.57 %		\	\	\

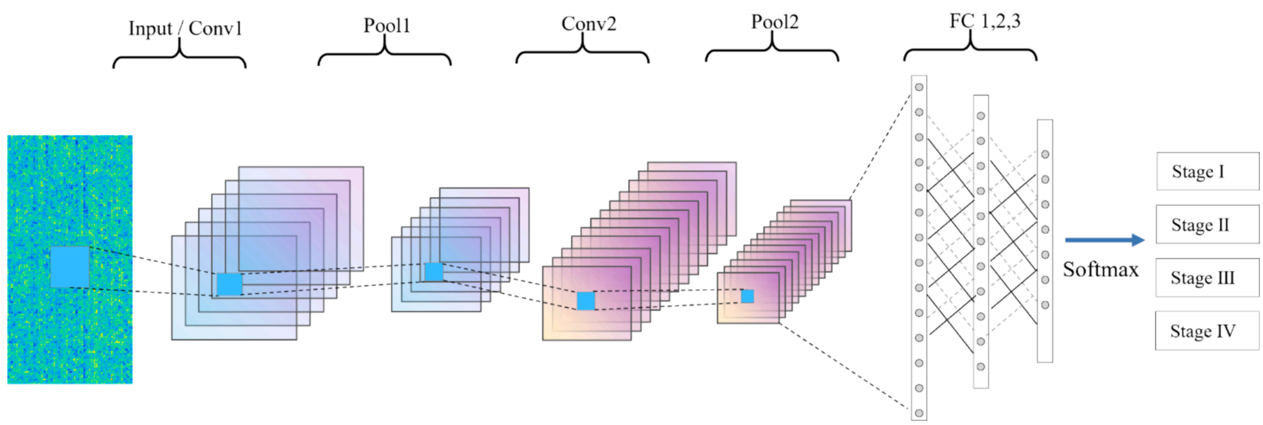

Fig. 5. Schematic diagram of CNN model for rock damage state identification.

the image.

In this study, we design an innovative CNN model called RDES-CNN (Fig. 5) specifically for identifying and analyzing rock damage evolution states. The model adopts a multi-layered structural design, including multiple Convolutional layers (Conv), multiple Maximum Pooling layers (Pool), and multiple Fully connected layers (FC layer). The characteristics of this model are as follows:

Specialized Handling of Temperature Matrix Data: Traditional deep learning models are usually designed to handle data types such as images, text, or audio. However, temperature matrix data has a unique two-dimensional structure that does not conform to the input format expected by traditional models. Therefore, we designed the RDES-CNN model specifically to handle temperature matrix data. RDES-CNN is optimized for the structural characteristics of temperature matrix data, enabling it to fully utilize the feature information and thereby enhance the performance of multi-classification tasks.

Multi-layer Feature Extraction Structure: The RDES-CNN model adopts a multi-layer structural design, including multiple convolutional layers, pooling layers, and fully connected layers. This structural arrangement allows the model to effectively process the complex infrared temperature matrix of rock, extracting key features layer by layer, and ultimately achieving accurate classification and identification of damage states.

Introduction of ReLU Activation Function: To enhance the model's ability to express nonlinear features, we introduced the ReLU activation function after each convolution operation and between the fully connected layers. According to the research of Krizhevsky et al. [61], the ReLU function can not only alleviate the problem of gradient disappearance but also accelerate the convergence speed of the network, thereby improving the training efficiency of the model.

Application of Average Pooling Layer: In the RDES-CNN model, we chose the average pooling layer. The reason for this choice lies in the unique advantages of the average pooling layer in handling noise. Average pooling effectively smooths the feature maps by calculating the average value of all values in the local region, reducing the interference of noise in feature extraction. This is crucial for accurately identifying the infrared radiation temperature damage areas of the rock, as changes in the damage state may manifest as slight variations in the overall temperature rather than just local prominent features.

Ingenious Addition of Dropout Layers: To further improve the model's generalization ability and avoid overfitting, we ingeniously added Dropout layers between the fully connected layers. During training, Dropout technology forces the network to learn more robust feature representations by randomly "dropping" the activation values of some neurons, thereby maintaining good recognition performance on unseen data.

Through these innovative features, the RDES-CNN model demonstrates significant advancements and unique advantages in handling temperature matrix data, effectively performing multi-classification tasks for rock damage evolution states.

3.3.3. Hyperparameter selection and optimization

To improve the performance of RDES-CNN in the classification task of rock damage state recognition, we use the grid search algorithm to optimize the hyperparameters to maximize the classification accuracy of the model. Fig. 6 is the pseudo-code of grid search. When implementing a grid search, it is first necessary to define a parameter space H, i.e., the set of all parameters of interest and their possible values. The algorithm then traverses this parameter space for every possible combination of parameters. For each set of parameters H, the algorithm uses a cross-validation approach to evaluate the model performance. Cross-validation is a statistical method for assessing the generalization ability of a machine learning model by partitioning a dataset to reduce bias in the assessment of the model's performance on an independent dataset.

In this paper, we use five-fold cross-validation, i.e., the dataset is divided into five equal-sized subsets, and each time, one of the subsets is used as the test set and the remaining four are used as the training set, and this process is repeated five times, and each time, a different subset is selected as the test set, so as to obtain the five model performance evaluation results, and finally, the average of the results of these five evaluations is taken as the performance metrics of the current parameter combination.

Several key hyperparameters are considered in the search process, including the number of convolutional kernels, the number of convolutional layers, the number of hidden layers, the Dropout rate, the learning rate, and the momentum of stochastic gradient descent (SGD). Specifically, the candidate values for the number of convolutional kernels are 8, 16, and 32, the candidate values for the number of convolutional layers are from 2 to 6, the candidate values for the number of hidden layers range from 32 to 1024, the candidate values for the Dropout rate are 0.3, 0.5, and 0.7, the candidate values for the Learning rate are 0.0001, 0.001, and 0.003, and the candidate values for the Momentum of SGD are 0.9, 0.95, and 0.99. In order to ensure that the optimal parameter combinations found are statistically stable and reliable, a 5-fold cross-validation method was used to evaluate each parameter combination. This means that each parameter combination is used to train the model 5 times, each time using a different division of the training and validation sets, thus reducing the chance of the results.

In this way, a total of 10,125 calculations were performed, as there were 2025 (i.e., 5 number of convolutional kernels × 5 number of convolutional layers × 5 number of hidden layers × 3 Dropout rate × 3 learning rate × 3 momentum) possible parameter combinations. After this exhaustive series of searches and validations, Table 4 demonstrates the best hyperparameter combination found by the lattice search algorithm, which results in a model accuracy of 0.997.

Algorithm 1 Grid Search with 5-Fold Cross-Validation

```
Initialize hyperparameter space H
Initialize best_params, best_score
for each set of hyperparameters h in H do
    Split training data into 5 folds
    for each fold do
        Train model with hyperparameters h on 4 folds
        Validate model on the remaining fold
        Calculate validation score
    end for
    Calculate average validation score over 5 folds
    if average score > best_score then
        Update best_score, best_params
    end if
end for
```

Fig. 6. Pseudo-code of grid search algorithm.

Table 4
RDES-CNN hyperparameter optimization results.

Hyper Parameter	Possible values	Best value	Train time	ACC
No. of Convolution & pool layers	[2,3,4,5,6]	2	17.53 s	0.997
No. of filters	[8,16,32]	8		
FC layer Output dimension	[64,128,256,512,1024]	128		
Dropout rate	[0.3,0.5,0.7]	0.3		
Learning rate	[0.0001,0.001,0.003]	0.003		
Moment of SGD	[0.9,0.95,0.99]	0.99		

3.3.4. Model parameters after RDES-CNN hyperparameter optimization

Fig. 5 shows the architecture of the model after parameter optimization, which first consists of convolutional layer 1 (Conv 1), which is responsible for receiving a single channel rock IR temperature matrix of dimension 200x100x1 as input data. At this stage, the model performs local feature extraction by applying eight 3x3 convolutional kernels, while a zero-padding technique is used to keep the spatial dimension of the output constant, i.e., 200x100x64, which helps to retain more feature information.

Subsequently, the model proceeds to the Pooling Layer 1 (Pool 1), where the feature map undergoes spatial downsampling through the application of Average Pooling. This method reduces the size of the feature map by half, resulting in a new dimension of 50x25x8. This step is intended to reduce the computational burden on the subsequent layers, and to extract higher-level abstract features by reducing the spatial resolution of the feature map.

Immediately after that, Convolutional Layer 2 (Conv 2) continues to process the feature maps obtained in the previous step. This layer also employs a 3x3 convolution kernel and keeps the number of output channels as 8, while maintaining the feature map size constant, i.e., 50x25x8, through a zero-padding strategy. Doing so further enriches the representation of the features and enhances the model's understanding of the rock IR temperature matrix data.

Through Pooling Layer 2 (Pool 2), the model further downsamples the feature map and compresses it to 25x12x8. This step helps in further extracting and compressing the key feature information while reducing the data dimensions.

Subsequently, the feature map undergoes a spreading operation to convert the multidimensional feature map into a one-dimensional vector, ready for the input of the fully connected (FC) layer. The fully connected layer consists of three parts: the FC1 layer maps the high-dimensional feature vectors to a new 128-dimensional feature space, the FC2 layer continues the dimensionality reduction process of the features to 128 dimensions, and the final FC3 layer maps the feature vectors to the final 4-dimensional outputs representing the different classes.

In order to improve the generalization ability of the model and prevent overfitting, a Dropout layer is added between the fully connected layers, and the Dropout rate is all set to 0.3. This strategy forces the network to learn a more robust representation of the features by randomly discarding a portion of the neurons' activation values during the training process. The design of the model fully considers the characteristics of the rock infrared temperature matrix data, and through the effective combination of convolutional and pooling layers, it realizes the efficient extraction and expression of the feature information in the temperature matrix.

3.3.5. Methodology and metrics

The schematic diagram of the framework developed in this research is shown in Fig. 7. First, noise removal is performed on the experimentally obtained infrared temperature data to extract the effective infrared radiation information during the coal rock loading process. Then, the experimental data are divided into training, validation, and testing

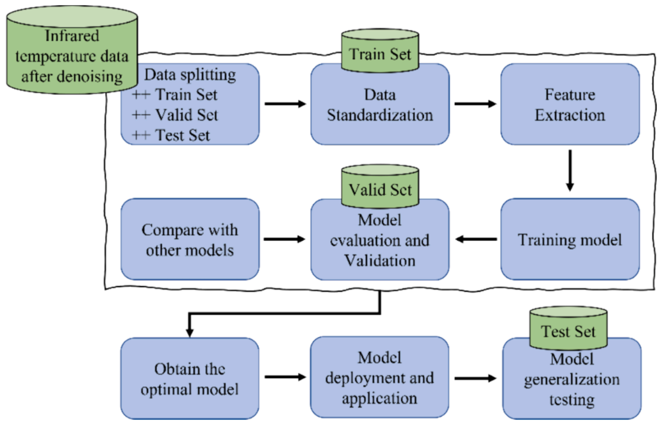

Fig.7. Proposed methodological framework.

datasets, and data normalization is executed before training starts. During training, feature extraction is performed on the training dataset, and the extracted features are used to classify and recognize the damage state of the coal rock.

In order to comprehensively evaluate the performance of the model, the model was evaluated using methods such as accuracy (ACC), precision, recall, F1-score, and confusion matrix. The calculation formulas are as follows:

$$Acc = \frac{TP + TN}{TP + TN + FN} \tag{9}$$

$$Precision = \frac{TP}{TP + FP} \tag{10}$$

$$\mathrm{Recall} = \frac{TP}{TP + FN} \tag{11}$$

$$F1 - score = \frac{2*Precision*\mathrm{Recall}}{Precision + \mathrm{Recall}} \tag{12}$$

Among them, ACC represents the proportion of correct predictions out of all samples. Precision represents the probability that a predicted category is correctly identified among all predicted results. Recall represents the probability that a category is correctly predicted among all true values. F1-score represents the harmonic mean of Precision and Recall. TP indicates that the prediction is positive and the actual is positive. FP indicates that the prediction is positive and the actual is negative. FN indicates that the prediction is a counterexample and the actual is a positive example, and TN indicates that the prediction is a counterexample and the actual is a counterexample. The confusion matrix is a visual matrix of statistical model classification performance, which shows TP, FP, FN, and TN of model classification.

4. Classification and identification of rock damage evolution states

4.1. Experimental setup

On the Ubuntu Serve20.04 operating system, the pytorch deep learning framework (version 1.13.1) is used to train on the graphics card model Tesla T4. The mini-batch size is set to 64. Using the stochastic gradient descent optimization algorithm, the momentum is 0.99, the initial learning rate is 0.003, and the loss function is the cross entropy loss function.

In the data preprocessing stage, through random sampling of the rock infrared temperature matrix data, we obtained the statistical parameters required for data normalization: the mean value is 0.05, and the variance is 0.24. Before inputting the data into the model, we standardize it so that the mean of each feature is 0 and the variance is 1. This preprocessing method helps to improve the training efficiency of the model and ensures that the model can converge to the optimal solution faster.

To improve the generalization ability of the model and prevent overfitting, we introduce an early stopping strategy during the training process. This strategy is implemented by monitoring the model's loss on the validation set, evaluating the model performance at the end of each epoch, and stopping the training if the performance does not show significant improvement. We set the training to be terminated if the model's performance on the validation set does not improve significantly within 10 consecutive epochs. This strategy helps us save computational resources and ensures that the final model has good generalization performance on new data.

4.2. Dataset settings

All the temperature matrices of A_1, B_2, C_3, and D_4 groups of samples are used as pre-test data sets for the generalization test after model training. For the remaining samples, 80 % of the temperature matrix of each damage state is used as the training set, and the other 20 % is used as the verification set for model training. The training model obtained at the end of the training will identify the damage state of the four groups of samples A_1, B_2, C_3, and D_4.

4.3. Baseline methodology

In this paper, we compare RDES-CNN with traditional machine learning algorithms, including support vector machines (SVM), K-nearest neighbors (KNN), random forests (RF), logistic regression (LR), and gradient boosting trees (GBT). First, we loaded and preprocessed the rock infrared temperature matrix dataset to convert the temperature matrix data into a feature representation that can be used by traditional machine learning algorithms. Specifically, each temperature matrix was spread into a one-dimensional feature vector, and these feature vectors were normalized, i.e., the processed features had a mean of 0 and a variance of 1. Normalization helps to ensure that the weights between different features are not dominated by differences in the scale of the data, thus improving the training stability and performance of the models. We then trained and evaluated each classification algorithm separately, and used the grid search algorithm as well as fivefold cross-validation to find the optimization of the hyperparameter combination for each classification model, and the value ranges of each parameter are shown in Table 5.

As can be seen in Table 5, the SVM, KNN, and LR models show excellent classification performance with an accuracy close to 0.984 on the validation dataset during the optimization process. The RF and GBT models, although slightly lower in performance, still provide acceptable accuracy. The KNN model takes only 1.89 s to train, showing great efficiency. In contrast, the SVM, RF, and LR models all took between 20 and 430 s to train, while the GBT model took the longest time at 15451.49 s. In comparison with the RDES-CNN model in Table 4, although the training time of the RDES-CNN is at a medium level, its recognition result on the validation set is the best, reaching 0.997. This is unmatched by other baseline models.

After obtaining the optimal parametric model, the model is trained on the full training dataset and the validation dataset. And compared with the RDES-CNN model, see subsection 4.5.

4.4. RDES-CNN calculation results

During the model training process, we recorded the loss values for each training and validation session and calculated the overall accuracy, F1-score, and confusion matrix for the validation sessions. As shown in Fig. 8(a), the Loss curve represents the entire training and validation process of the RDES-CNN. Fig. 8 (b) depicts the accuracy and F1-score

Table 5
Hyperparameter optimization results of other models.

Method	Parameters of the classification method	Possible values	Best value	Train time	ACC
SVM	C: Regularization parameter	[0.1, 1, 10]	0.1	425.64 s	0.9836
	Kernel parameter of the RBF kernel function	[1, 0.1, 0.01]	\		
	Kernel type	['rbf', 'linear']	'linear'		
RF	Number of trees	[10, 50, 100]	100	29.37 s	0.9687
	The maximum depth of the decision tree	[None, 10, 20]	20		
	Minimum number of samples required to split internal nodes	[2,5,10]	2		
	Minimum number of samples required on leaf nodes	[1,2,4]	1		
GBT	number of estimators	[50, 100, 200]	200	15451.49 s	0.9859
	learning rate	[0.01, 0.1, 0.5]	0.5		
	maximum depth of a single tree	[3,5,7]	3		
KNN	number of neighbors	[3,5,10]	3	1.89 s	0.9859
	neighbor weight calculation method	['uniform', 'distance']	'uniform'		
	nearest neighbor search algorithm	['auto', 'ball_tree', 'kd_tree', 'brute']	'ball_tree'		
LR	regularization term	['l1', 'l2']	'l2'	20.63 s	0.9836
	reciprocal of regularization strength	[0.1, 1, 10]	10		

curves of the RDES-CNN on the validation set, while Fig. 8 (c) shows the confusion matrix of the RDES-CNN on the validation set.

From Fig. 8 (a), it is evident that the model converged rapidly from the beginning, and after approximately 20 epochs, both the validation and training losses stabilized around their respective minimum values. Simultaneously, the accuracy and F1-score also reached stable values (Fig. 8 (b)). During the model training process, we employed an early stopping strategy. Throughout the 500 training sessions, the model's loss stabilized at the 45th epoch, achieving an accuracy of 0.9891 and an F1-score of 0.9893. As shown in Fig. 8 (c), the RDES-CNN performed excellently in recognizing the four damage states. Therefore, the model corresponding to the 45th epoch is used as the model for identifying the damage evolution states of coal rock in this study.

4.5. Comparison results of RDES-CNN with other models

In this study, we comparatively analyze the performance of RDES-CNN and baseline methods on the validation set. Table 6 demonstrates the performance of RDES-CNN with other baseline methods on the dataset. The RDES-CNN model exhibits excellent performance in key performance metrics such as Accuracy (ACC), Precision, Recall, and F1 score. Specifically, the accuracy of RDES-CNN reaches 99.04 %, while the Precision, Recall, and F1 scores are all close to or above 99 %, which to a certain extent reflects the model's efficiency and reliability in the classification task.

In contrast, other models such as SVM and LR also performed well in terms of accuracy, with both achieving 99.39 % accuracy, which is comparable to RDES-CNN. However, RDES-CNN shows a more balanced and consistent performance in terms of precision, recall, and F1-score, ostensibly providing more stable and accurate results when dealing with more rocky damage state classification recognition problems. In addition, RF, GBT, and KNN models, although they also perform well in some indicators, do not reach the level of RDES-CNN in terms of overall performance. Therefore, we can assume that RDES-CNN has a more outstanding performance on the validation set, especially in terms of precision rate, recall rate, and F1 score. This indicates that RDES-CNN has stronger classification ability and higher prediction accuracy.

4.6. Model generalizability test

The comparative results of the RDES-CNN model as well as the baseline model for damage evolution state identification on the four sets

Table 6
Performance of RDES-CNN and other models on the validation set.

Model	Performance of the model on the verification set			
	ACC ↑	Precision↑	Recall↑	F1-score↑
RDES-CNN	0.9904	**0.9939**	**0.9952**	**0.9946**
SVM	**0.9939**	**0.9939**	0.9944	0.9942
RF	0.9555	0.9609	0.9519	0.9559
GBT	0.9747	0.9745	0.9737	0.9740
KNN	0.9915	0.9910	0.9918	0.9913
LR	**0.9939**	**0.9939**	0.9944	0.9939

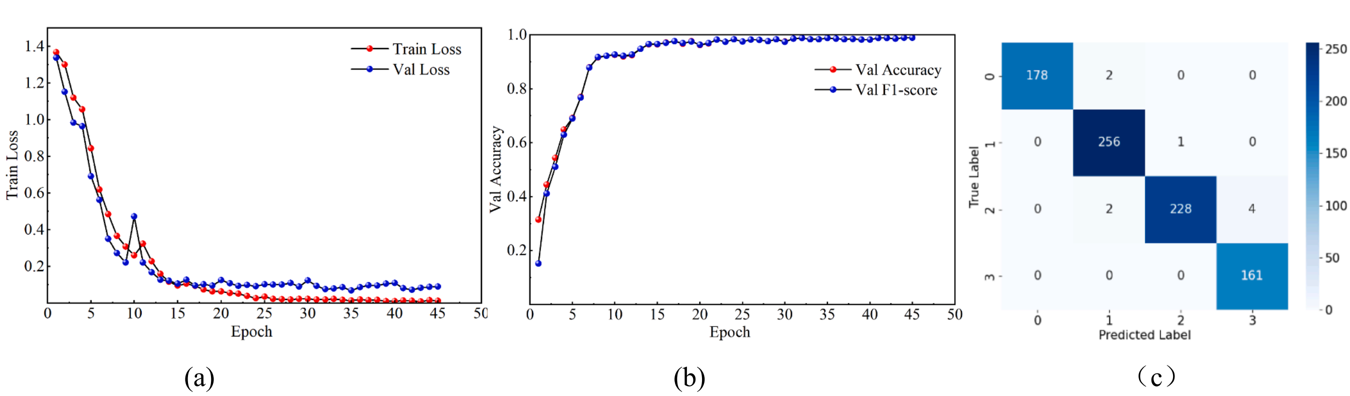

Fig. 8. Results of model calculation in training set and validation set: (a) Plots of Loss curves, (b) Accuracy curves and F1-score curves for training and validation set, (c) Model confusion matrix in validation set.

of rock sample datasets that were not involved in training are presented in Table 7. Throughout the experiments, RDES-CNN shows relatively high performance in terms of accuracy and F1-score, especially on specimen A_1 and specimen C_3. Compared with other models, RDES-CNN achieves better recognition results in most cases. For example, on specimen A_1, the accuracy of RDES-CNN is 0.6168, while that of the other models is 0.4147 (SVM), 0.2680 (RF), 0.4611 (GBT), 0.2530 (KNN), and 0.3802 (LR), respectively. This demonstrates the superiority and generalization ability of RDES-CNN in dealing with the task of identifying the evolutionary state of damage in rock samples. Although other models also show some performance in some cases, overall, RDES-CNN is a relatively better choice for this task, indicating that the RDES-CNN model has strong generalization performance.

Fig. 9 presents the confusion matrices for the RDES-CNN and SVM models on the four test samples (A_1, B_2, C_3, D_4). In these matrices, 0, 1, 2, and 3 represent stage I, stage II, stage III, and stage IV respectively. It is evident from the figure that RDES-CNN consistently outperforms SVM in terms of recognition accuracy for all test samples.

Further analysis shows that RDES-CNN has a stronger recognition capability for stage I damage across all test samples compared to other stages. This indicates that the model is particularly effective in extracting features from the infrared temperature matrix of stage I damage. However, the performance for stage II and stage III suggests that the model requires further optimization. The results indicate that RDES-CNN has learned many overlapping features between these two stages, making it difficult for the model to distinguish between them. To address this issue, it is necessary to increase the dataset size for stages II, III, and IV and implement measures in feature enhancement and model fine-tuning to improve the model's learning and differentiation capabilities.

In conclusion, while the RDES-CNN model demonstrates superior overall performance compared to the SVM model, a detailed analysis of the confusion matrices reveals specific areas for improvement to enhance its generalization ability and recognition accuracy across all damage stages. This will be further discussed in Section 5.2.

5. Discussion

5.1. Advantages of infrared radiation identification of rock damage evolution state

When the rock is subjected to loading, the internal primary cracks, micro-pores, and regenerated cracks and pores will gradually develop. This process has gone through four stages of development: initial compaction stage, elastic deformation stage, plastic deformation stage and post-peak failure stage. Different damage states lead to different degrees of the spatial and temporal evolution of internal micropores and fissures so the infrared radiation information of rock surface shows differences at different damage stages, which can be observed intuitively from Fig. 3 and Fig. 4.

Through infrared radiation monitoring technology, we can capture the infrared radiation information released by the rock during the damage process. By using convolutional neural networks to extract features from this information, we can effectively recognize the damaged state of rocks. In this paper, this intelligent identification method is validated on a small-scale dataset, which provides a feasible idea for future applications in online real-time identification of rock damage states.

The intelligent recognition method using deep learning and infrared radiation monitoring technology avoids the tedious calculation steps and the judgment error of human subjective factors in traditional methods (such as the strain method). At the same time, compared with the limitations of traditional methods that cannot achieve real-time determination, this method can achieve real-time damage state determination in the actual engineering site and has great advantages. Therefore, this paper provides an intelligent method based on infrared radiation technology, which provides an effective way for the monitoring and identification of rock damage state and has important academic and practical significance for engineering practice.

5.2. Research gaps and prospects

As far as is known, the dataset for recognizing the state of rock damage evolution based on infrared radiation technology has not been reported. This may be because scientists in rock mechanics are more interested in the mechanical properties of rock materials, and the study of rock damage evolution based on infrared radiation technology has received little attention. On the other hand, artificial intelligence scientists typically pay little attention to rock infrared radiation images. Therefore, based on the uniaxial monitoring experiment of rock infrared radiation, it is necessary to establish a dataset for the identification of rock damage evolution states. The database established in this paper contains four kinds of rocks: yellow shale, limestone, yellow sandstone, and coal, which is of reference significance for the laboratory study of general coal-bearing rocks. In future research, the database can be expanded and improved in the following four aspects: ① Expansion of rock types. ② Increase in the number of samples for each type of rock. ③ Improvement in the quality of IR images, specifically the denoising of rock IR images. ④ Enhancement of the classification method for rock damage evolution stages.

In this study, infrared radiation monitoring technology and deep convolutional neural network methods are used to classify and predict the damage state of four different rocks, yielding good recognition results. The main contribution of this paper is the application of infrared radiation technology and deep learning methods to identify and assess the evolution of rock damage states. This approach applies to infrared radiation monitoring and early warning in indoor experiments, and it holds reference significance for practical field applications. During the process of rock loading failure, the surface thermal radiation is directly related to the stress state. Since stress is a time-dependent variable, changes in infrared radiation on the rock surface are related to the duration of loading time [41,49,62]. As shown in Figs. 3 and 4, the surface infrared radiation of the four rocks has changed significantly in both the time and space dimensions. However, the RDES-CNN used in this paper can only extract features from rock IR images in the spatial dimension. Therefore, the model does not consider time variation characteristics. In future research, both the time and space variation characteristics can be taken into account to identify the rock damage

Table 7
Performance of the model on the test dataset.

Model	A_1		B_2		C_3		D_4	
	ACC↑	F1-score↑	ACC↑	F1-score↑	ACC↑	F1-score↑	ACC↑	F1-score↑
RDES-CNN	**0.6168**	**0.6551**	**0.5780**	**0.5329**	**0.6490**	**0.6335**	**0.5034**	**0.4544**
SVM	0.4147	0.4642	0.3366	0.3830	0.4471	0.4772	0.2054	0.2266
RF	0.2680	0.3324	0.3220	0.3599	0.3639	0.4062	0.2559	0.2998
GBT	0.4611	0.5347	0.4439	0.5019	0.4698	0.4870	0.4024	0.4286
KNN	0.2530	0.2797	0.2756	0.2733	0.1641	0.1675	0.2155	0.2543
LR	0.3802	0.4271	0.2098	0.2693	0.3769	0.4108	0.1145	0.1188

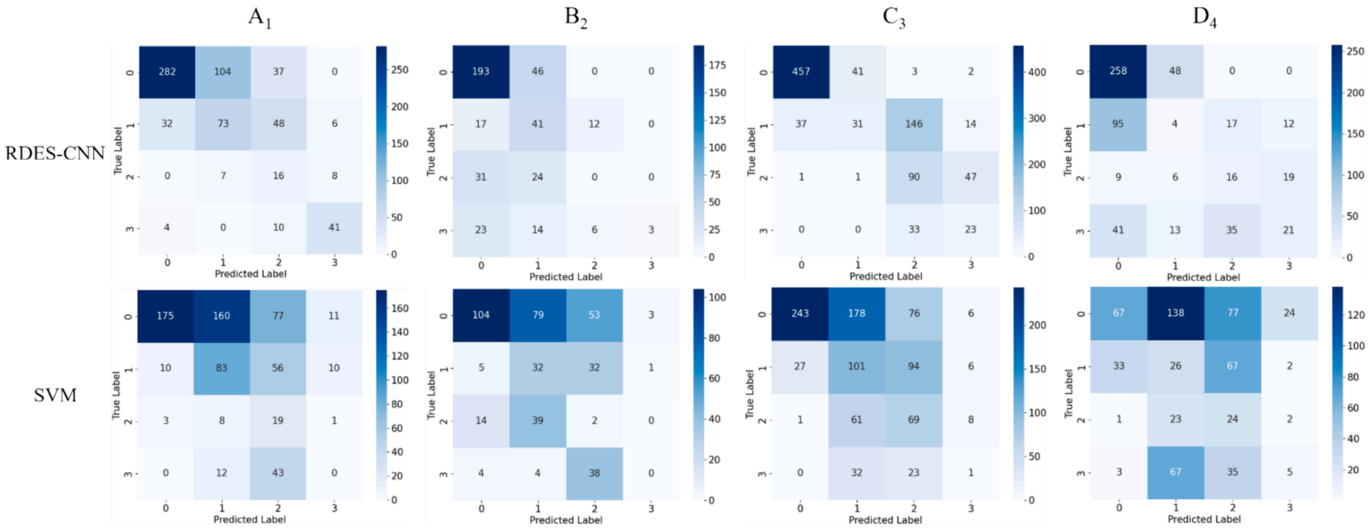

Fig. 9. Identification results of RDES-CNN and SVM in test samples.

state. For example, recurrent neural networks (RNN) and long short-term memory networks (LSTM) can be used for recognition. This approach can further improve the deep learning model for rock damage evolution state recognition.

6. Conclusion

This study successfully identified the damage evolution states in various rocks using infrared radiation monitoring technology and deep learning methods. The main conclusions are as follows:

(1) The changes in infrared radiation information at various stages of damage evolution in different rocks exhibit similarities.
(2) A dataset method for identifying coal rock damage states using infrared radiation information was proposed, and the dataset imbalance was addressed through downsampling.
(3) The intelligent damage state identification model, RDES-CNN, demonstrates excellent performance, with both accuracy and F1-scores exceeding 90 %. This shows its general applicability for damage identification across various samples.
(4) The proposed method of using infrared radiation technology for the intelligent identification of bearing coal rock damage states is feasible. This method holds significant importance for safety monitoring in geotechnical and mining engineering.

CRediT authorship contribution statement

Qiangqiang Gao: Writing – original draft, Software, Methodology, Funding acquisition, Formal analysis, Data curation, Conceptualization. **Liqiang Ma:** Writing – review & editing, Supervision, Software, Resources, Project administration, Funding acquisition, Conceptualization. **Wei Liu:** Writing – review & editing, Software, Formal analysis, Data curation. **Hui Wang:** Writing – review & editing, Validation, Formal analysis. **Qiang Ma:** Writing – review & editing, Supervision, Software, Resources, Project administration, Funding acquisition, Conceptualization. **Xiuzhe Wang:** Writing – review & editing, Formal analysis.

Declaration of competing interest

The authors declare that they have no known competing financial interests or personal relationships that could have appeared to influence the work reported in this paper.

Data availability

Data will be made available on request.

Acknowledgments

This paper was supported by the National Natural Science Foundation of China (51874280), the Fundamental Research Funds for the Central Universities (2021ZDPY0211), the Research and Engineering Demonstration of Low Cost Large Scale Purification and Cascade Utilization Technology for Mining Brackish Water in the Zhundong Region (2023B03009), the Postgraduate Research & Practice Innovation Program of Jiangsu Province (KYCX23_2811), and the Graduate Innovation Program of China University of Mining and Technology (2023WLKXJ046).

References

[1] Y. Zhang, W. Wu, X. Yao, P. Liang, B. Tian, Y. Huang, J. Liang, Acoustic emission-infrared characteristics and damage evolution of granite under uniaxial compression, Rock Soil Mech. 41 (2020) 139–146.
[2] J. Dai, J. Liu, L. Zhou, X. He, Crack pattern recognition based on acoustic emission waveform features, Rock Mech. Rock Eng. 56 (2023) 1063–1076.
[3] X. Zhang, X. Li, Y. Liu, W. Liu, Q. Li, L. Li, Experimental study on crack propagation and failure mode of fissured shale under uniaxial compression, Theor. Appl. Fract. Mech. 121 (2022) 103512.
[4] Q. Zhang, X. Li, J. Gao, S. Jia, X. Ye, Macro-and meso-damage evolution characteristics of coal using acoustic emission and keuence testing technique, Nat. Resour. Res. 31 (2022) 517–534.
[5] S. Song, T. Ren, L. Dou, J. Sun, X. Yang, L. Tan, Fracture features of brittle coal under uniaxial and cyclic compression loads, Int. J. Coal Sci. Technol. 10 (2023) 9.
[6] W. Hou, D. Ma, Q. Li, J. Zhang, Y. Liu, C. Zhou, Mechanical and hydraulic properties of fault rocks under multi-stage cyclic loading and unloading, Int. J. Coal Sci. Technol. 10 (2023) 54.
[7] N. Erarslan, Investigation of the fracture process zone and behavior of the macro-scale fatigue cracks in brittle rock specimens, Rock Soil Mech. 44 (2023) 4.
[8] X. Chengyu, L. Weihang, C. Ziwei, W. Yabin, Study on the infrared dynamic evolution characteristics of different joint inclination phyllite under uniaxial compression, Sci. Rep. 13 (2023) 9867.
[9] X. Li, H. Li, Z. Yang, H. Zuo, W. Sun, H. Li, Y. Li, Coupling mechanism of dissipated energy-infrared radiation energy of the deformation and fracture of composite coal-rock under load, ACS Omega 7 (2022) 8060–8076.
[10] T. Zhao, P. Zhang, Y. Xiao, W. Guo, Y. Zhang, X. Zhang, Master crack types and typical acoustic emission characteristics during rock failure, Int. J. Coal Sci. Technol. 10 (2023).
[11] S. Yin, Z. Li, E. Wang, X. Li, H. Tian, Y. Niu, Infrared temperature evolution law and thermal effect mechanism of concrete impact failure, J. Build. Eng. 91 (2024) 109592.
[12] Z. Yuan, F. Ren, D. Liu, Experimental investigation on the infrared precursors of rockburst in sandstone with different bedding dip angles, Infrared Phys. Technol. 128 (2023).

[13] P. Xie, W. Chen, W. Zhao, H. Gao, Acquisition of acoustic emission precursor information for rock masses with a single joint based on clustering-convolutional neural network method, J. Rock Mech. Geotech. Eng. (2024).
[14] S. Wang, Y. Zhao, J. Guo, B. Liu, Investigation on prediction of sandstone failure under uniaxial compression based on supervised deep learning, Rock Mech. Rock Eng. 56 (2023) 8485–8501.
[15] B. Li, E. Wang, Z. Li, X. Cao, X. Liu, M. Zhang, Automatic recognition of effective and interference signals based on machine learning: a case study of acoustic emission and electromagnetic radiation, Int. J. Rock Mech. Min. Sci. 170 (2023) 105505.
[16] Y. Di, E. Wang, Z. Li, X. Liu, T. Huang, J. Yao, Comprehensive early warning method of microseismic, acoustic emission, and electromagnetic radiation signals of rock burst based on deep learning, Int. J. Rock Mech. Min. Sci. 170 (2023) 105519.
[17] Z. Song, Y. Wu, Y. Zhang, Y. Yang, Z. Yang, Mechanical responses and acoustic emission behaviors of coal under compressive differential cyclic loading (DCL): a numerical study via 3D heterogeneous particle model, Int. J. Coal Sci. Technol. 10 (2023) 31.
[18] S. Zhang, D. Zhang, G. Feng, M. Chi, Modelling method of heterogeneous rock mass and DEM investigation of seepage characteristics, Geomech. Geophys. Geo-Energy Geo-Resour. 10 (2024) 46.
[19] C. Martin, N. Chandler, The progressive fracture of Lac du Bonnet granite, Elsevier, International journal of rock mechanics and mining sciences & geomechanics abstracts, 1994, pp. 643–659.
[20] E. Eberhardt, D. Stead, B. Stimpson, R.S. Read, Identifying crack initiation and propagation thresholds in brittle rock, Can. Geotech. J. 35 (1998) 222–233.
[21] M. Tang, G. Wang, S. Chen, C. Yang, An objective crack initiation stress identification method for brittle rock under compression using a reference line, Rock Mech. Rock Eng. 54 (2021) 4283–4298.
[22] F. Amann, Ö. Ündül, P.K. Kaiser, Crack initiation and crack propagation in heterogeneous sulfate-rich clay rocks, Rock Mech. Rock Eng. 47 (2014) 1849–1865.
[23] X. Zhao, M. Cai, J. Wang, L. Ma, Damage stress and acoustic emission characteristics of the Beishan granite, Int. J. Rock Mech. Min. Sci. 64 (2013) 258–269.
[24] X. Li, G. Si, J. Oh, I. Canbulat, Z. Xiang, T. Li, A pre-peak elastoplastic damage model of gosford sandstone based on acoustic emission and ultrasonic wave measurement, Rock Mech. Rock Eng. 1–20 (2022).
[25] L. Dong, Y. Chen, D. Sun, Y. Zhang, Implications for rock instability precursors and principal stress direction from rock acoustic experiments, Int. J. Min. Sci. Technol. 31 (2021) 789–798.
[26] A. Cao, G. Jing, Y.-L. Ding, S. Liu, Mining-induced static and dynamic loading rate effect on rock damage and acoustic emission characteristic under uniaxial compression, Saf. Sci. 116 (2019) 86–96.
[27] K. Zhao, H. Ma, X. Liang, X. Li, Y. Liu, R. Cai, L. Ye, C. Yang, Damage evaluation of rock salt under multilevel cyclic loading with constant stress intervals using AE monitoring and CT scanning, J. Pet. Sci. Eng. 208 (2022) 109517.
[28] X. Zeng, H. Liu, H. Zhu, C. Ling, K. Liang, H. Umar, Y. Xie, G. Long, C. Ma, Study on damage of concrete under uniaxial compression based on electrical resistivity method, Constr. Build. Mater. 254 (2020) 119270.
[29] Y. Yang, Y. Li, J. Yao, K. Zhang, S. Iglauer, L. Luquot, Z. Wang, Formation damage evaluation of a sandstone reservoir via pore-scale X-ray computed tomography analysis, J. Pet. Sci. Eng. 183 (2019) 106356.
[30] J. He, M. Serati, M. Veidt, A. De Alwis, Determining rock crack stress thresholds using ultrasonic through-transmission measurements, Int. J. Coal Sci. Technol. 11 (2024) 19.
[31] G. Zhang, F. Gao, Z. Wang, S. Yue, S. Deng, Quantifying the progressive fracture damage of granite rocks by stress-strain, acoustic emission, and active ultrasonic methods, J. Mater. Civ. Eng. 33 (2021).
[32] W. Liu, L.Q. Ma, H. Sun, N.M. Khan, An experimental study on infrared radiation and acoustic emission characteristics during crack evolution process of loading rock, Infrared Phys. Technol. 118 (2021) 103864.
[33] A. Kravcov, E. Cherepetskaya, P. Svoboda, D. Blokhin, P. Ivanov, I. Shibaev, Thermal infrared radiation and laser ultrasound for deformation and water saturation effects testing in limestone, Remote Sens. (Basel) 12 (2020) 4036.
[34] X. Li, J. Bu, Z. Yang, H. Li, J. Zhou, Z. Liu, Y. Wang, The law of infrared radiation generation and evolution of coal rock fracture under load, Infrared Phys. Technol. (2024) 105338.
[35] H. Sun, H.-Y. Zhu, J. Han, C. Fu, M.-M. Chen, K. Wang, Energy and infrared radiation characteristics of the sandstone damage evolution process, Materials 16 (2023).
[36] C. Zhang, S. Jia, Y. Zhao, S. Fang, Z. Ren, J. Liu, Weakening mechanism and infrared radiation characteristics of coal with different moisture contents in the brazilian test, Int. J. Geomech. 24 (2024).
[37] W. Liu, L. Ma, Q. Gao, H. Wang, Y. Fang, Q. Ma, H. Sun, Z. Zhang, Failure precursors recognition method for loading coal and rock using the fracture texture features of infrared thermal images, Infrared Phys. Technol. 139 (2024) 105319.
[38] W. Liu, L. Ma, Q. Gao, A.J.S. Spearing, Y. Wang, R. Cui, Z. Zhao, Fracture precursor recognition and damage quantitative characterization of stressed rock using infrared radiation, Rock Mech. Rock Eng. (2023).
[39] C. Lwab, B. Sl, B. Yw, A. Cw, Precursors for rock fracturing and failure—Part I: IRR image abnormalities, Int. J. Rock Mech. Min. Sci. 43 (2006) 473–482.
[40] L.X. Wu, S.J. Liu, Y.H. Wu, C.Y. Wang, Precursors for rock fracturing and failure—Part II: IRR T-curve abnormalities, Int. J. Rock Mech. Min. Sci. 43 (2006) 483–493.
[41] C.L. Wang, Z.J. Lu, L. Liu, X.S. Chuai, H. Lu, Predicting points of the infrared precursor for limestone failure under uniaxial compression, Int. J. Rock Mech. Min. Sci. 88 (2016) 34–43.
[42] Z.H. Li, Q. Lou, E.Y. Wang, S.J. Liu, Y. Niu, Study on acoustic-electric-heat effect of coal and rock failure processes under uniaxial compression, J. Geophys. Eng. 15 (2018) 71–80.
[43] M.Z. Huo, Y.Y. Xia, X.Q. Liu, M.Q. Lin, Z.D. Wang, W.H. Zhu, Evolution characteristics of temperature fields of rockburst samples under different stress gradients, Infrared Phys. Technol. 109 (2020) 103425.
[44] M. Lin, C. Gao, Y. Xia, D. Zhang, X. Liu, X. Liang, Rock burst initiation and precursors in a model specimen based on acoustic emission and infrared monitoring, Arab. J. Geosci. 15 (2022) 333.
[45] Z.H. Li, H. Tian, Y. Niu, E.Y. Wang, X. Zhang, S. He, F.Z. Wang, A.Q. Zheng, Study on the acoustic and thermal response characteristics of coal samples with various prefabricated crack angles during loaded failure under uniaxial compression, J. Appl. Geophys. 200 (2022) 104618.
[46] Z.H. Li, S. Yin, Y. Niu, F.Q. Cheng, S.J. Liu, Y.H. Kong, Y.H. Sun, Y. Wei, Experimental study on the infrared thermal imaging of a coal fracture under the coupled effects of stress and gas, J. Nat. Gas Sci. Eng. 55 (2018) 444–451.
[47] K. Cao, L. Ma, D. Zhang, X. Lai, Z. Zhang, N.M. Khan, An experimental study of infrared radiation characteristics of sandstone in dilatancy process, Int. J. Rock Mech. Min. Sci. 136 (2020) 104503.
[48] W. Liu, L.Q. Ma, H. Sun, N.M. Khan, Using the characteristics of infrared radiation b-value during the rock fracture process to offer a precursor for serious failure, Infrared Phys. Technol. 114 (2021) 103644.
[49] R.X. Shen, H.R. Li, E.Y. Wang, T.Q. Chen, T.X. Li, H. Tian, Z.H. Hou, Infrared radiation characteristics and fracture precursor information extraction of loaded sandstone samples with varying moisture contents, Int. J. Rock Mech. Min. Sci. 130 (2020).
[50] X. Liu, H. Wang, H. Jing, A. Shao, L. Wang, Research on intelligent identification of rock types based on faster R-CNN method, IEEE Access 8 (2020) 21804–21812.
[51] L. Si, X. Xiong, Z. Wang, C. Tan, A deep convolutional neural network model for intelligent discrimination between coal and rocks in coal mining face, Math. Prob. Eng. (2020) 1–12.
[52] H. Sun, W. Du, C. Liu, Uniaxial compressive strength determination of rocks using X-ray computed tomography and convolutional neural networks, Rock Mech. Rock Eng. 54 (2021) 4225–4237.
[53] A. Baghbani, T. Choudhury, S. Costa, J. Reiner, Application of artificial intelligence in geotechnical engineering: a state-of-the-art review, Earth Sci. Rev. 228 (2022) 103991.
[54] H. Sun, L.Q. Ma, N. Adeleke, Y. Zhang, Background thermal noise correction methodology for average infrared radiation temperature of coal under uniaxial loading, Infrared Phys. Technol. 81 (2017) 157–165.
[55] W.L. Gong, Y.X. Gong, A.F. Long, Multi-filter analysis of infrared images from the excavation experiment in horizontally stratified rocks, Infrared Phys. Technol. 56 (2013) 57–68.
[56] Q. Gao, L. Ma, W. Liu, K. Cao, N.M. Khan, Z. Zhao, Appraisal of rock IR law and damage precursor: insight infrared thermogram entropy, Infrared Phys. Technol. (2022) 104443.
[57] Q. Gao, L. Ma, W. Liu, N.M. Khan, S.S. Alarifi, M. Sazid, W.B. Inqiad, Method for rock fracture prediction and early warning: Insight from fusion of multi-physics field information, Heliyon 10 (2024).
[58] Z. Bieniawski, Mechanism of brittle fracture of rock: part II—experimental studies, Int. J. Rock Mechanics and Mining Sciences & Geomechanics Abstracts, Elsevier (1967) 407–423.
[59] Z.T. Bieniawski, Mechanism of brittle fracture of rock: part I—theory of the fracture process, Int. J. Rock Mechanics and Mining Sciences & Geomechanics Abstracts, Elsevier (1967) 395–406.
[60] M. Cai, P.K. Kaiser, Y. Tasaka, Generalized crack initiation and crack damage stress thresholds of brittle rock masses near underground excavations, Int. J. Rock Mech. Min. Sci. 41 (2004).
[61] A. Krizhevsky, I. Sutskever, G.E. Hinton, ImageNet classification with deep convolutional neural networks, Commun. ACM 60 (2017) 84–90.
[62] X.M. Sun, H.C. Xu, M.C. He, F. Zhang, Experimental investigation of the occurrence of rockburst in a rock specimen through infrared thermography and acoustic emission, Int. J. Rock Mech. Min. Sci. 93 (2017) 250–259.